Materials Advances

ROYAL SOCIETY OF CHEMISTRY

PAPER

View Article Online
View Journal | View Issue

Cite this: *Mater. Adv.*, 2021, 2, 4824

Energy transfer-triggered multicolor emissions in Tb^{3+}/Eu^{3+}-coactivated $Y_2Mo_3O_{12}$ negative thermal expansion microparticles for dual-channel tunable luminescent thermometers†

Peng Du, * Laihui Luo, Yafei Hou and Weiping Li

A rational control of the thermal quenching performance is crucial for achieving high quality luminescent thermometers. Herein, we report the synthesis of Tb^{3+}/Yb^{3+}-coactivated $Y_2Mo_3O_{12}$ (YMO) negative thermal expansion (NTE) microparticles with color-tunable emissions. Upon irradiation with 297 nm light, multicolor emissions (green-yellow-red) are observed in the developed samples which are trigged by efficient energy transfer (ET) from the Tb^{3+} to Eu^{3+} ions. Furthermore, according to the theoretical analysis based on the decay time and Inokuti–Hirayama model, the aforementioned ET mechanism is related to the dipole–quadrupole interaction. Owing to the NTE behaviors of the YMO host, ET between Tb^{3+} and Eu^{3+} ions is enhanced, causing them to possess diverse thermal quenching properties. Employing the fluorescence intensity ratio technology, the thermometric behaviors of the developed microparticles were investigated by discussing the temperature-dependent emission intensities of Tb^{3+} and Eu^{3+} ions. It is found that the sensitivities of the designed NTE microparticles are dependent on both the doping concentration and excitation wavelength. Additionally, the maximum absolute and relative sensitivities of YMO:Tb^{3+}/0.10Eu^{3+} NTE microparticles are 0.017 K^{-1} and 0.32% K^{-1}, respectively, at 363 K. These results reveal that the developed NTE microparticles have the capacity for contactless thermometry and their thermometric behaviors can be controlled by adjusting the doping content and excitation wavelength.

Received 11th March 2021,
Accepted 10th June 2021

DOI: 10.1039/d1ma00218j

rsc.li/materials-advances

1. Introduction

Optical thermometers based on rare-earth ion-activated luminescent materials have attracted much attention because of their advantages including high resolution, non-contact characteristic, and fast response.[1–3] Generally, by taking advantage of the various thermal quenching performances of two emissions originating from thermally coupled levels (*i.e.*, TCLs) of rare-earth ions, ratiometric thermometry can be realized by utilizing the fluorescence intensity ratio (*i.e.*, FIR) technology.[4,5] Based on the temperature-dependent emission intensities of the $^2H_{11/2}$ and $^4S_{3/2}$ TCLs of Er^{3+} ions, Zhang *et al.* discovered that the absolute sensitivity (*i.e.*, S_a) of $Gd_{9.33}(SiO_4)_6O_2$:Er^{3+}/Yb^{3+} phosphors was 0.00464 K^{-1}.[6] M. Runowski *et al.* reported that the maximum relative sensitivity (*i.e.*, S_r) of YVO_4:Tm^{3+}/Yb^{3+} nanoparticles was around 2.9% K^{-1} when the $^3F_{2,3}$ and $^3H_4$ TCLs of Tm^{3+} ions were utilized.[7] However, optical thermometers based on the TCLs of rare-earth ions exhibit some limitations, such as low S_r (*i.e.*, $S_r = \Delta E/kT^2$) value given that it is proportional to the energy gap ($200 \leq \Delta E \leq 2000$ cm^{-1}) of TCLs and unsatisfactory accuracy, which is caused by the overlapped emissions arising from TCLs.[8,9] Inspired by these features, some facile approaches should be developed to boost the thermometric properties of luminescent materials doped with rare-earth ions.

Currently, to eliminate the limitation of the energy gap of TCLs on the thermometric behaviors of optical thermometers, researchers have proposed a new route, namely, utilizing the temperature-dependent FIR of two luminescent centers.[10,11] Through the use of the temperature-dependent FIR values of Bi^{3+} and Eu^{3+} ions, Jeong *et al.* found that the S_a and S_r values of Bi^{3+}/Eu^{3+}-coactivated $GdNbO_4$ phosphors were as high as 0.0367 K^{-1} and 3.81% K^{-1}, respectively.[12] Based on the diverse thermal quenching behaviors of Mn^{2+} and Mn^{4+} ions in $ZnGa_{2-y}Al_yO_4$, You *et al.* reported that the studied samples exhibited high maximum S_r values of 4.345% K^{-1}.[13] Besides, this technique was also employed to investigate the temperature sensing capacity of other compounds, such as $LiTaO_3$:Ti^{4+}/Eu^{3+} (S_a = 0.671 K^{-1}; S_r = 5.425% K^{-1}), $Lu_3Al_5O_{12}$:Ce^{3+}/Mn^{4+}

Department of Microelectronic Science and Engineering, School of Physical Science and Technology, Ningbo University, 315211 Ningbo, Zhejiang, China. E-mail: dp2007good@sina.com, dupeng@nbu.edu.cn

† Electronic supplementary information (ESI) available. See DOI: 10.1039/d1ma00218j

(S_r = 4.37% K^{-1}), $SrGdLiTeO_6$:Mn^{4+}/Eu^{3+} (S_r = 4.9% K^{-1}), and $NaLuF_4$:Eu^{3+}@g-C_3N_4 (S_a = 0.0057 K^{-1}; S_r = 0.455% K^{-1}).[14–17] Notably, when the FIR strategy based on dual-emitting centers is employed, superior S_a and S_r values can be obtained in rare-earth ion-coactivated luminescent materials, implying that the utilization of the various thermal responses of dual-emitting centers is an efficient route to achieve high thermometric properties.

As is known, the temperature sensing capacity of luminescent materials is impacted by the host matrix, and thus, selecting a proper host will be a good method to enhance the thermometric properties of optical thermometers. Recently, there is an increasing interest in compounds with negative thermal expansion (NTE) performances, in which their unit cell decreases with an increase in temperature, given that they can be used to adjust the thermal expansion coefficient of other compounds.[18,19] Furthermore, it was revealed that the upconversion emission intensities of rare-earth ion-doped NTE samples, such as $Sc_2Mo_3O_{12}$:Ho^{3+}/Yb^{3+} and $Yb_2W_3O_{12}$:Er^{3+}/Yb^{3+}, were greatly improved at elevated temperature because of the thermally enhanced energy transfer (ET) between the sensitizer and activator.[20,21] Thus, NTE compounds are potential luminescent hosts for rare-earth ions. Among them, $Y_2Mo_3O_{12}$ (YMO), which belongs to the $A_2M_3O_{12}$ family with intense NTE properties, has been widely researched to modify the thermal expansion coefficient of composites.[22,23] However, to the best of our knowledge, investigations on the luminescent and thermometric properties of rare-earth ion-activated YMO are rare. Herein, rare-earth ions of Tb^{3+} and Eu^{3+} were selected as the research objects given that they not only emit bright green and red emissions, respectively, but also can realize ET from the Tb^{3+} to Eu^{3+} ions.[24,25] With the help of the sol–gel technique, a series of Tb^{3+}/Eu^{3+}-coactivated YMO NTE microparticles with multicolor emissions were prepared and their phase structure, morphology, decay time and luminescent behaviors were explored. Furthermore, *via* use of the lifetime and Inokuti–Hirayama model, the ET mechanism between the Tb^{3+} and Eu^{3+} ions in the YMO host lattices was theoretically studied, which was confirmed to be determined by dipole–quadrupole interaction. Additionally, the temperature monitoring capacity of the resultant NTE microparticles was investigated by analyzing the diverse thermal quenching performances of the Tb^{3+} and Eu^{3+} ions. Ultimately, we also explored the impact of doping concentration and excitation wavelength on the thermometric behaviors of the designed compounds.

2. Experimental

2.1 Synthesis of Tb^{3+}/Eu^{3+}- coactivated YMO microparticles

$Y_{1.94-2x}Mo_3O_{12}$:0.06Tb^{3+}/2xEu^{3+} (YMO:Tb^{3+}/2xEu^{3+}; $0 \le x \le 0.09$) NTE microparticles were synthesized by employing a traditional sol–gel method. Herein, raw materials including $(NH_4)_6Mo_7O_{24}\cdot 4H_2O$ (99.9%), $Tb(NO_3)_3\cdot 6H_2O$ (99.9%), $Y(NO_3)_3\cdot 6H_2O$ (99.99%), citric acid (98%) and $Eu(NO_3)_3\cdot 6H_2O$ (99.99%) were employed to prepare the designed compounds. In brief, firstly, the proper amounts of $Y(NO_3)_3\cdot 6H_2O$ ((1.94 − 2x) mmol), $Er(NO_3)_3\cdot 5H_2O$ (0.03 mmol), $Yb(NO_3)_3\cdot 5H_2O$ (2x mmol) and $(NH_4)_6Mo_7O_{24}\cdot 4H_2O$ (0.143 mmol) powder were weighed and put in a beaker containing 200 mL of deionized water. Afterwards, citric acid (10 mmol) was weighed and put into the above-mentioned solution and strongly stirred to dissolve them. Then, the beaker was sealed with a lid and heated at 80 °C for 30 min. Then, the lid was shifted, and it was continually heated at 80 °C to evaporate the water to form a wet-gel. Subsequently, the wet-gel was kept in an oven and heated at 120 °C to form a xerogel. Finally, the xerogel was transferred to a furnace and sintered at 800 °C for 6 h to obtain the final products. Herein, the heating rate was kept as 5 °C min^{-1} to achieve the calcinating temperature of 800 °C.

2.2 Characterization

The final products were characterized *via* X-ray diffractometry (Bruker D8 Advance; Cu Kα radiation with a fixed wavelength of 1.5406 Å), field-emission scanning electron microscopy (FE-SEM; HITACHI SU3500) equipped with energy-dispersive X-ray spectroscopy (EDS), Fourier transform infrared (FT-IR) spectroscopy (Bruker Tensor 27), microfluorescence spectroscopy (Ocean Optics QE pro), differential scanning calorimetry and thermogravimetric analysis (DSC-TG) (SDTQ 600). The excitation and emission spectra of the studied NTE microparticles were recorded using a fluorescence spectrometer (Edinburgh FS5), in which a temperature controlling system (Linkam HFS600E-PB2) was attached. Additionally, the decay time of the resultant NTE microparticles was examined using a fluorescence spectrometer (Edinburgh FS1000).

3. Results and discussion

3.1 Phase structure and microstructure behaviors

The crystal structure and phase purity of the developed NTE microparticles were examined *via* X-ray diffraction (XRD). Fig. 1(a) illustrates the XRD profiles of the YMO:Tb^{3+}/2xEu^{3+} ($0 \le x \le 0.09$) NTE microparticles and the standard XRD data of YMO. It is evident that the detected diffraction peaks of the samples match well with that of the standard YMO (JCPDS# 28-1454), revealing that the dopants (*i.e.*, Tb^{3+}, Eu^{3+}) were successfully incorporated into the YMO host lattices and the final products have a pure orthorhombic phase. In an attempt to comprehend the phase compositions of the designed compounds, their typical Raman spectra were measured, as shown in Fig. 1(b). As presented, the Raman spectra are dominated by three bands at 323.7, 821.5 and 957.3 cm^{-1}, which coincide well with the previously reported Raman modes of the orthorhombic YMO.[22] In particular, the two peaks centered at 957.3 and 821.5 cm^{-1} are associated with the symmetric and asymmetric stretching vibrations of the MoO_4 tetrahedron, respectively, whereas the band at 323.7 cm^{-1} is assigned to the asymmetric and symmetric bending motions in both the YO_6 octahedron and MoO_4 tetrahedron.[22] Thus, according to these characteristics, it can be concluded that the dopants are successfully introduced into the YMO host lattices and the resultant

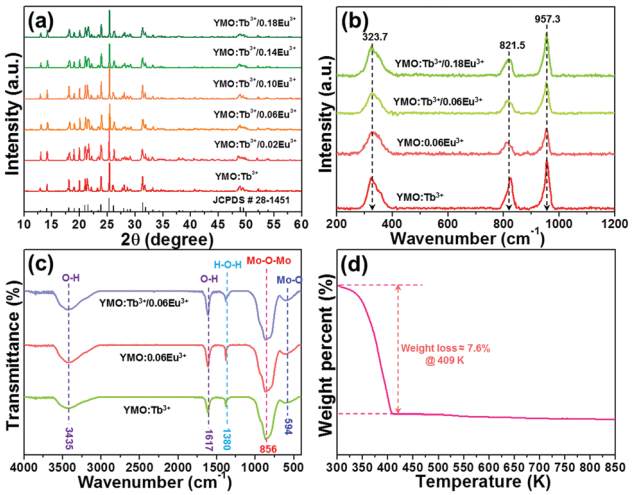

Fig. 1 (a) XRD patterns of YMO:Tb^{3+}/2xEu^{3+} ($0 \leq x \leq 0.09$) NTE microparticles. (b) Raman spectra of YMO:Tb^{3+}/2xEu^{3+} (x = 0, 0.03, 0.09) and YMO:0.06Eu^{3+} NTE microparticles. (c) FT-IR spectra of YMO:Tb^{3+}, YMO:0.06Eu^{3+} and YMO:Tb^{3+}/0.06Eu^{3+} NTE microparticles. (d) TG spectrum of YMO:Tb^{3+}/0.06Eu^{3+} NTE microparticles.

NTE microparticles present a pure orthorhombic crystal structure.

The FT-IR spectra of YMO:Tb^{3+}, YMO:0.06Eu^{3+} and YMO:Tb^{3+}/0.06Eu^{3+} NTE microparticles were measured and demonstrated in Fig. 1(c). As disclosed, all the samples show the same FT-IR profiles, and their absorption signals are independent of the doping concentration and dopant type. The absorption bands at 3435 and 1617 cm^{-1} are ascribed to the O–H symmetric stretching vibration, whereas the band at 1380 cm^{-1} corresponds to the H–O–H blending vibration.[26] Notably, the obtained O–H and H–O–H vibrations reveal the existence of water on the surface of the resultant NTE microparticles. Apart from these absorption bands, two other bands located at 856 and 594 cm^{-1}, which are assigned to the Mo–O–Mo and Mo–O stretching vibration modes, respectively, were also detected.[26] The thermal stability of the resultant compounds was explored to confirm their feasibility for application in a high temperature environment, as demonstrated in Fig. 1(d). It is confirmed in Fig. 1(d) that the weight of the samples presents a decline trend due to the evaporation of water when the temperature is less than 409 K, leading to the weight loss of around 7.6%. Nevertheless, the weight of the NTE microparticles remains constant with a further increase in temperature (*i.e.*, over 409 K), manifesting the splendid thermal stability of the developed products.

The morphology of the prepared samples was characterized *via* FE-SEM. The FE-SEM image in Fig. 2(a) shows the presence of amorphous microparticles, which are triggered by the high-temperature sintering process. Furthermore, the shape and size of the microparticles are also determined to be independent of the Eu^{3+} ion concentration, as shown in Fig. S1 (ESI†). Specifically, the particle size of YMO:0.06Eu^{3+}, YMO:Tb^{3+}, YMO:Tb^{3+}/0.01Eu^{3+}, YMO:Tb^{3+}/0.05Eu^{3+}, YMO:Tb^{3+}/0.07Eu^{3+} and YMO:Tb^{3+}/0.09Eu^{3+} is calculated to be 4.57, 42.7, 4.30, 4.43, 4.26 and 4.48 μm, respectively, as presented in Fig. S3 (ESI†). The EDS was employed to detect the elemental composition of the studied samples. It can be seen that the final products are composed of Y, Mo, O, Tb and Eu elements (Fig. 2(b)). Additionally, the elemental mapping results verify that these elements are uniformly distributed in the synthesized compounds, as displayed in Fig. 2(c)–(h).

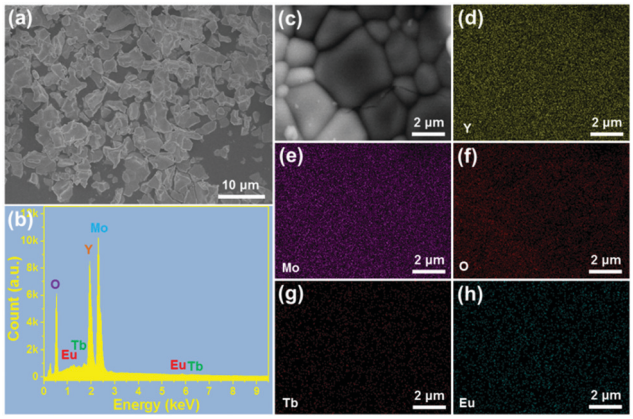

Fig. 2 (a) FE-SEM image, (b) EDS spectrum, and (c)–(h) elemental mapping of YMO:Tb^{3+}/0.06Eu^{3+} NTE microparticles.

3.2 Optical properties of the resultant microparticles

To analyze the ET process in the YMO:Tb^{3+}/2xEu^{3+} NTE microparticles, we measured the excitation and emission spectra of three typical compounds including YMO:Tb^{3+}, YMO:0.06Eu^{3+} and YMO:Tb^{3+}/0.06Eu^{3+} NTE microparticles, as presented in Fig. S3 (ESI†). The detected excitation and emission spectra reveal that the ET exists in the YMO:Tb^{3+}/2xEu^{3+} NTE microparticles (see ESI†). To get deeper insight into the ET process and the luminescent behaviors of the final products, the emission spectra of the YMO:Tb^{3+}/2xEu^{3+} NTE microparticles excited by 297 nm were recorded, as demonstrated in Fig. 3(a). Apparently, all the samples emit the emissions of the Tb^{3+} and Eu^{3+} ions, in which their intensities are impressively impacted by the Eu^{3+} ion concentration. Specifically, a monotonous decreasing tendency in the emission intensity of the Tb^{3+} ion was seen, whereas the Eu^{3+} ions showed the opposite changing trend (see Fig. S4, ESI†), further proving the existence of ET from the Tb^{3+} to Eu^{3+} ions in the studied samples. Considering that the Tb^{3+} and Eu^{3+} ions present various changing tendencies in emission intensity, the colorific performance of the as-prepared compounds is demonstrated to be dependent on the doping content. The CIE coordinates of the YMO:Tb^{3+}/2xEu^{3+} NTE microparticles were computed, as illustrated in Fig. 3(b) and Table S1 (ESI†). With a change in the Eu^{3+} ion concentration in the range of $0 \leq x \leq 0.09$, the color coordinates of the samples are tuned from (0.328,0.566) to (0.614,0.355), namely, multicolor emissions could be realized. Notably, the emitting-color of the YMO:Tb^{3+}/2xEu^{3+} NTE microparticles gradually changes from green to yellow, and finally to red with an increase in the Eu^{3+} ion content (see Fig. 3(b)). Besides the CIE coordinates, we also explored the correlated color

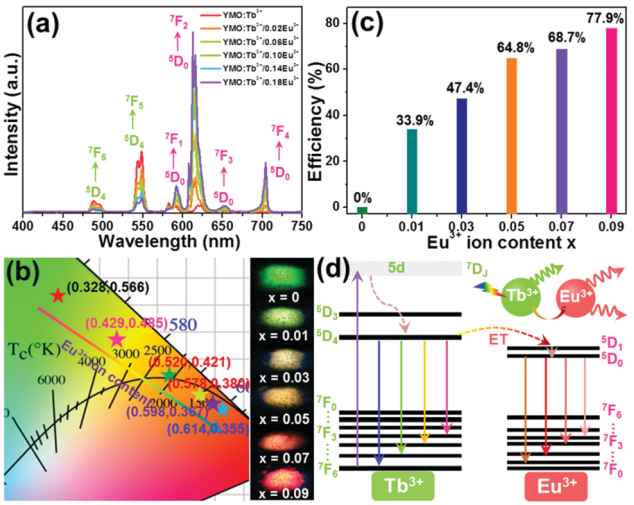

Fig. 3 (a) Emission spectra and (b) CIE chromaticity diagram and optical images of YMO:Tb^{3+}/2xEu^{3+} ($0 \leq x \leq 0.09$) NTE microparticles. (c) ET efficiency as a function of Eu^{3+} ion content. (d) Simplified energy level diagram describing the ET process in the YMO:Tb^{3+}/2xEu^{3+} NTE microparticles.

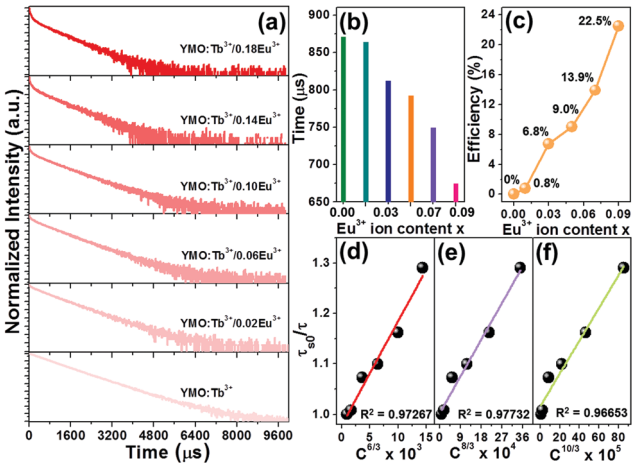

Fig. 4 (a) Decay profiles of YMO:Tb^{3+}/2xEu^{3+} NTE microparticles. Dependence of (b) lifetime and (c) ET efficiency on the Eu^{3+} ion concentration. Dependence of (τ_{s0}/τ) of Tb^{3+} ions on (d) $C^{6/3} \times 10^3$, (e) $C^{8/3} \times 10^4$ and (f) $C^{10/3} \times 10^5$ for YMO:Tb^{3+}/2xEu^{3+} NTE microparticles.

temperature (CCT) of the emissions *via* use of the following expressions:[27,28]

$$\mathrm{CCT} = -437n^3 + 3601n^2 - 6846n + 5514.31 \quad (1)$$

$$n = (x - x_e)/(y - y_e) \quad (2)$$

where $(x_e, y_e) = (0.3320, 0.1858)$ and (x, y) are associated with the CIE coordinates of the detected emissions. Thus, based on these two functions and the calculated CIE coordinates, the CCT values of the emissions were estimated, as displayed in Table S1 (ESI†). Apparently, the CCT values changed in the range of 1713–5587 K with a change in the Eu^{3+} ion concentration (see Table S1, ESI†). Furthermore, to quantitatively describe the aforementioned ET, its efficiency (*i.e.*, η) was determined by utilizing the formula $\eta = (1 - I_S/I_{S0}) \times 100\%$ (where I_S and I_{S0} denote the fluorescent intensities of the Tb^{3+} ions with and without Eu^{3+} ions, respectively).[29,30] As disclosed, the η value is dependent on the doping content and reached the maximum value of 77.9% when $x = 0.09$ (see Fig. 3(c)), revealing that the ET between the Tb^{3+} and Eu^{3+} ions is efficient. Additionally, the calculated critical distance (*i.e.*, $R_c = 32.04$ Å) confirms that the ET mechanism belongs to the multipolar interaction, as shown in Fig. S5 (see ESI†). The involved luminescent and ET processes are summarized in Fig. 3(d).

To further prove the existence of ET in the resultant microparticles, the decay curves of the Tb^{3+} ions in the YMO:Tb^{3+}/2xEu^{3+} NTE microparticles ($\lambda_{ex} = 378$ nm and $\lambda_{em} = 548$ nm) were examined, as shown in Fig. 4(a). As disclosed, the decay curves of the YMO:Tb^{3+} compounds match a single exponential decay mode as follows:

$$I(t) = I_0 \exp(-t/\tau) + A \quad (3)$$

where I_0 and $I(t)$ show the fluorescence intensities at time $t = 0$ and t, respectively, A is a coefficient and τ refers to the lifetime. Thus, the lifetime of the Tb^{3+} ions in the YMO:Tb^{3+} compounds was proved to be 870.7 μs. However, with the introduction of Eu^{3+} ions, the recorded decay curves of the YMO:Tb^{3+}/2xEu^{3+} NTE microparticles ($x > 0$) diverges from the single exponential decay mode and they could only be fitted using a non-exponential decay mode, as follows:[16,31]

$$\tau_m = \frac{\int_0^\infty t \times I(t)\mathrm{d}t}{\int_0^\infty I(t)\mathrm{d}t} \quad (4)$$

where $I(t)$ has the same meaning as presented in eqn (3) and τ_m is the decay time. The calculated decay time is shown in Fig. 4(b). Obviously, the lifetime of the Tb^{3+} ions becomes shorter and shorter with an increasing in the Eu^{3+} ion content due to the ET from the Tb^{3+} to Eu^{3+} ions.[32] Furthermore, it is widely accepted that the ET efficiency between the sensitizer and activator can also be estimated from the decay time using the following expression:[33,34]

$$\eta = \left(1 - \frac{\tau_s}{\tau_{s0}}\right) \times 100\% \quad (5)$$

where τ_s and τ_{s0} are associated with the lifetimes of the Tb^{3+} ions with and without doped Eu^{3+} ions, respectively. Thus, using eqn (5) and the obtained lifetime, the ET efficiency was explored and displayed in Fig. 4(c). Fig. 4(c) shows that the η value is enhanced with an increment in the doping content, achieving the maximum value of 22.5%. These achievements directly confirm the efficient ET between the Tb^{3+} and Eu^{3+} ions in the YMO:Tb^{3+}/2xEu^{3+} NTE microparticles.

As discussed above, the ET mechanism pertains to multiple interactions. To comprehend the involved ET mechanism in depth, we employed the Inokuti–Hirayama (I–H) ET model to analyze the decay time. According to the I–H ET model, the

lifetime and fluorescence intensity maintain the following relationship:[35]

$$I(t) = I_0 \exp\left[-\frac{t}{\tau_0} - \frac{4}{3}\pi\Gamma\left(1-\frac{3}{s}\right)N_a R_0{}^3\left(\frac{t}{\tau_0}\right)^{3/s}\right] \quad (6)$$

where I_0 and $I(t)$ have the same meaning as that in eqn (3), τ_0 refers to the lifetime of the sensitizer without adding the activator, N_a is the number of activators, Γ denotes the gamma expression, and s has three different values of 6, 8 and 10, which are assigned to the dipole–dipole, dipole-quadrupole and quadrupole-quadrupole interactions, respectively. According to Fig. S6 (ESI†), the fitting result is the best when s = 8, manifesting that the dipole–quadrupole interaction leads to ET in the resultant compounds. Besides the I–H ET model, the exact ET mechanism can also be verified using the following function given by Dexter and Reisfeld:[36]

$$\frac{\tau_{s0}}{\tau_s} \propto C^{n/3} \quad (7)$$

where τ_s and τ_{s0} have the same meaning as that in eqn (6), C refers to the total content of Tb^{3+} and Eu^{3+} ions and the n value is determined by the type of ET mechanism, that is, the dipole–dipole, dipole-quadrupole and quadrupole-quadrupole interactions correspond to the n value of 6, 8 and 10, respectively. The plots of τ_{s0}/τ_s *vs.* $C^{n/3}$ are illustrated in Fig. 4(d)–(f). Notably, when n = 8, the fitting result is the best, clearly implying that the ET from Tb^{3+} to Eu^{3+} is realized by the dipole–quadrupole interaction.

3.3 Optical thermometric performance of the Tb^{3+}/Eu^{3+}-coactivated YMO microparticles

In an attempt to explore the temperature sensing capacity of the studied samples, their thermal evolution emission spectra were examined. The temperature-dependent emission spectra of the YMO:Tb^{3+}/0.06Eu^{3+} NTE microparticles excited at 297 nm are depicted in Fig. 5(a) and Fig. S7 (ESI†). As demonstrated, an increase in temperature has little effect on the luminescent profiles of the samples, whereas the emission intensities of the Tb^{3+} and Eu^{3+} ions are sensitive to the temperature. Fig. 5(b) shows that the thermal quenching effect is gained in both the Tb^{3+} and Eu^{3+} ions when the temperature is boosted to 363 K, and their emission intensities remain at about 47.3% and 84.7%, respectively, of their initial values at 163 K. Based on the literatures,[37,38] lattice shrinking will occur in the YMO host at elevated temperatures due to the NTE effect, leading to a decrease in the distance between the Tb^{3+} and Eu^{3+} ions and enhancement in the ET probability. Furthermore, the thermally enhanced ET can promote the Tb^{3+} ions to transfer more energy to the Eu^{3+} ions, resulting in a faster decline in the emission intensity of the Tb^{3+} ions than that of the Eu^{3+} ions at high temperature. Considering that the Tb^{3+} and Eu^{3+} ions exhibit diverse thermal quenching behaviors, their FIR (*i.e.*, I_{Eu}/I_{Tb}) values will be dependent on temperature. Fig. 5(c) shows the temperature-dependent FIR value of the YMO:Tb^{3+}/0.06Eu^{3+} NTE microparticles. Apparently, with the tuning of the temperature in the range of 163–363 K, a gradual increment is observed in the FIR value. It is widely acknowledged that the relation between temperature (*i.e.*, T) and FIR value that originates from two emitting centers obeys the following expression:[9,12]

$$\mathrm{FIR} = \frac{I_{Eu}}{I_{Tb}} = B\exp(-C/T) + D \quad (8)$$

where I_{Eu} and I_{Tb} are the luminescence intensities of the Eu^{3+} and Tb^{3+} ions, respectively, and B, C and D are coefficients. Using eqn (6), the temperature-dependent FIR value is well fitted, and the values of B, C and D were determined to be 12.20, 1019.08 and 1.85, respectively (Fig. 5(c)).

To explore the feasibility of the developed samples for ratiometric thermometry, their thermometric behaviors should be evaluated by studying their temperature-dependent sensitivity (*i.e.*, S_a and S_r). Herein, the exact S_a and S_r values were estimated by utilizing the following functions:[13,17]

$$S_a = \frac{d\mathrm{FIR}}{dT} = B\exp(-C/T) \times \frac{C}{T^2} \quad (9)$$

$$S_r = \frac{1}{\mathrm{FIR}}\frac{d\mathrm{FIR}}{dT} \times 100\% = \frac{B\exp(-C/T)}{B\exp(-C/T)+D} \times \frac{c}{T^2} \times 100\% \quad (10)$$

Thus, using these functions and the fitted values, the dependence of the S_a and S_r values on temperature was determined, as shown in Fig. 5(d). As disclosed, a gradual increasing tendency in both the S_a and S_r values is observed with an increase in temperature in the range of 163–363 K. Particularly, the maximum values are 0.0057 K^{-1} and 0.22% K^{-1}, respectively, when the temperature was 363 K. This result implies that the Tb^{3+}/Eu^{3+}-coactivated YMO NTE microparticles possess the capacity of temperature monitoring.

As proposed in previous reports,[37–39] some factors such as host, laser pump power, and dopant content can impact the

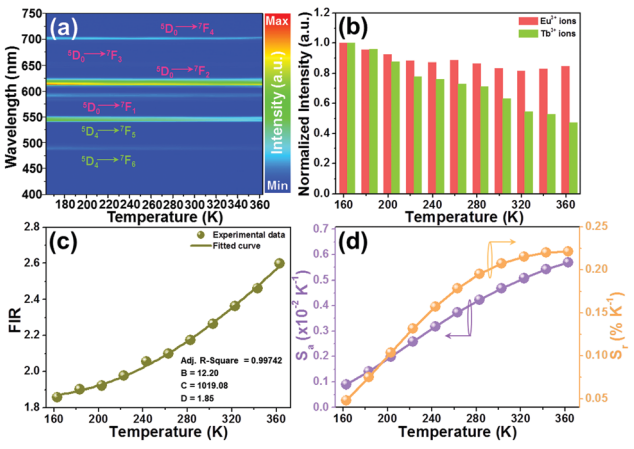

Fig. 5 (a) Thermal evolution emission spectra of YMO:Tb^{3+}/0.06Eu^{3+} NTE microparticles excited at 297 nm. (b) Normalized emission intensities of the Eu^{3+} and Tb^{3+} ions as a function of temperature. (c) Dependence of FIR value on temperature. (d) Temperature-dependent S_a and S_r values.

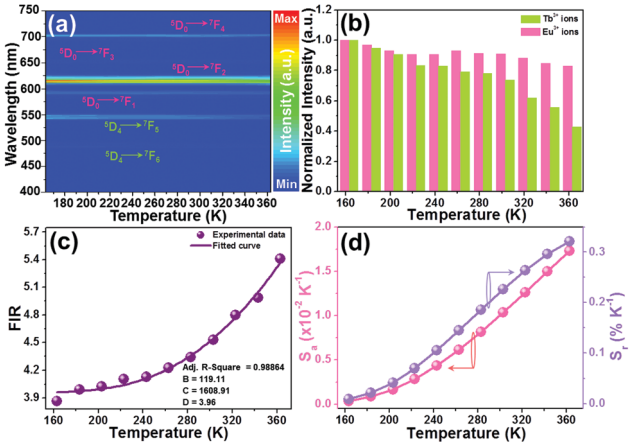

Fig. 6 (a) Thermal evolution emission spectra of YMO:Tb^{3+}/0.10Eu^{3+} NTE microparticles excited at 297 nm. (c) Normalized emission intensities of the Eu^{3+} and Tb^{3+} ions as a function of temperature. (d) Dependence of FIR value on temperature. (d) Temperature-dependent S_a and S_r values.

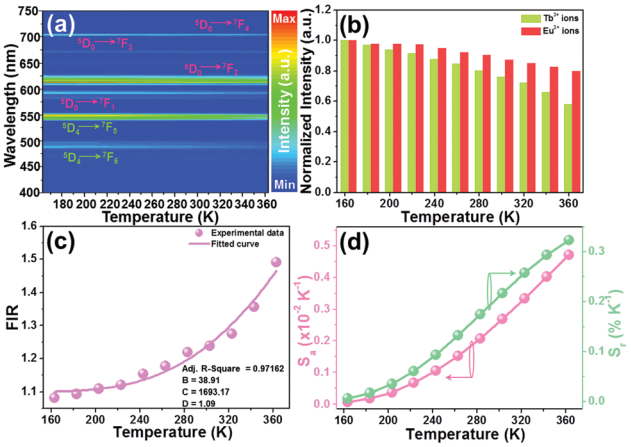

Fig. 7 (a) Thermal evolution emission spectra of YMO:Tb^{3+}/0.06Eu^{3+} NTE microparticles excited at 378 nm. (b) Normalized emission intensities of the Eu^{3+} and Tb^{3+} ions as a function of temperature. (c) Dependence of FIR value on temperature. (d) Temperature-dependent S_a and S_r values.

thermometric behaviors of rare-earth ion-activated luminescent materials. Herein, in an attempt to discover the impact of doping content (or emission intensity) on the temperature sensing capacity of the resultant NTE microparticles, we recorded the temperature-dependent emission spectra of the YMO:Tb^{3+}/2xEu^{3+} NTE microparticles with a doping content of 5 mol%, as depicted in Fig. 6(a) and Fig. S8 (ESI†). From the achieved emission spectra, it is evident that the thermal quenching behaviors also occurred in the YMO:Tb^{3+}/0.10Eu^{3+} NTE microparticles when the temperature increases from 163 to 363 K. Noteworthily, the emission intensity of the Tb^{3+} ions decreases faster than that of the Eu^{3+} ions (see Fig. 6(b)), which contributes to the temperature-dependent FIR values. As shown in Fig. 6(c), the FIR value of I_{Eu}/I_{Tb} increases from 3.87 to 5.41 in the temperature range of 163–363 K. Furthermore, these FIR values are in accordance with eqn (8), in which the values of B, C and D were determined to be 119.11, 1608.91 and 3.96, respectively. Additionally, the calculated S_a and S_r values using eqn (9) and (10), respectively, are demonstrated in Fig. 6(d). Significantly, both the S_a and S_r values are dependent on the temperature and their maximum values are 0.017 K^{-1} and 0.32% K^{-1}, respectively, when the temperature is 363 K. In comparison with that of the YMO:Tb^{3+}/0.06Eu^{3+} NTE microparticles, it can be seen the S_a and S_r values of the YMO:Tb^{3+}/0.10Eu^{3+} NTE microparticles are greatly increased, suggesting that the thermometric performance of the studied samples can be regulated through the modulation of the Eu^{3+} ion concentration. Notably, the sensitivities of the YMO:Tb^{3+}/0.10Eu^{3+} NTE microparticles are comparable with that of previously developed luminescent thermometers (see Table 1), which indicates the feasibility of the designed samples for application in optical thermometry.

Besides the doping content, the influence of excitation wavelength on the thermometric properties of the developed NTE microparticles was also explored. The temperature-dependent emission spectra of the YMO:Tb^{3+}/0.06Eu^{3+} NTE microparticles excited at 378 nm were recorded, as shown in Fig. 7(a) and Fig. S9 (ESI†). Although the resultant NTE microparticles still emit the featured emissions of the Tb^{3+} and Eu^{3+} ions when excited at 378 nm, their relative emission intensities are significantly changed compared with that excited at 297 nm, resulting in diverse FIR values of I_{Eu}/I_{Tb}. With an increase in temperature, the thermally induced florescence decrease phenomenon is observed and the emission intensities of the Tb^{3+} and Eu^{3+} ions also exhibited diverse changes with temperature, as described in Fig. 7(b). On account of the measured temperature-dependent emission spectra, the FIR

Table 1 Thermometric properties of thermometers based on rare-earth ion-activated luminescent materials

Luminescent materials	Temperature (K)	λ_{ex} (nm)	S_a (K^{-1})	S_r (K^{-1})	Ref.
$Gd_{9.33}(SiO_4)_6O_2$:Yb^{3+}/Er^{3+}	298–548	980	0.00464	—	6
Bi_5IO_7:Er^{3+}	303–543	980	0.0069	1.36%	8
$NaLuF_4$:Eu^{3+}@g-C_3N_4	303–503	394	0.0057	0.455%	17
$CaWO_4$:Yb^{3+}/Er^{3+}	298–625	980	0.0073	—	40
$Bi_4Ti_3O_{12}$:Yb^{3+}/Er^{3+}	293–573	980	0.0052	—	41
$Ca_3Al_2O_6$:Yb^{3+}/Er^{3+}	298–573	980	0.0078	—	42
Ca_2MgWO_6:Er^{3+}/Yb^{3+}	303–573	980	0.0092	0.82%	43
$KBaY(MoO_4)_3$:Yb^{3+}/Er^{3+}	250–460	980	0.01306	1.80%	44
YMO:Tb^{3+}/0.06Eu^{3+}	163–363	297	0.0057	0.22%	This work
YMO:Tb^{3+}/0.10Eu^{3+}	163–363	297	0.017	0.32%	This work
YMO:Tb^{3+}/0.06Eu^{3+}	163–363	378	0.0047	0.32%	This work

values at different temperatures were evaluated, as presented in Fig. 7(c). Fig. 7(c) shows that the FIR value exhibits an increasing trend with temperature and it can be well fitted by eqn (8), where the values of B, C and D are 38.91, 1693.17 and 1.09, respectively. The temperature-dependent S_a and S_r values of the YMO:Tb^{3+}/0.06Eu^{3+} NTE microparticles excited by 378 nm are depicted in Fig. 7(d). As disclosed, both the S_a and S_r values increased with an increase in temperature in the range of our interest, reaching the maximum values of 0.0047 K^{-1} and 0.32% K^{-1}, respectively, at 363 K, which are totally different from that of the samples excited by 297 nm (*i.e.*, S_a = 0.0057 K^{-1} and S_r = 0.22% K^{-1}). These results indicate that changing in the excitation wavelength is also an efficient route to modify the sensitivity of YMO:Tb^{3+}/2$x$$Eu^{3+}$ NTE microparticles besides the doping content.

4. Conclusion

In summary, YMO:Tb^{3+}/2$x$$Eu^{3+}$ NTE microparticles were synthesized to explore their promising applications in thermometers. Upon excitation at 297 nm, efficient ET from the Tb^{3+} to Eu^{3+} ions is observed in the prepared samples, leading to multicolor emissions, namely, from green to yellow and finally to red. Through theoretical calculation based on the decay time and I–H model, the involved ET mechanism is determined to be the dipole–quadrupole interaction. With aid of FIR technology, the potential applications of the resultant microparticles for thermometry are explored by discussing the temperature-dependent emission intensities of the Tb^{3+} and Eu^{3+} ions. It is found that the thermometric properties of the YMO:Tb^{3+}/2$x$$Eu^{3+}$ NTE microparticles can be adjusted by utilizing the dual-channels of changing the doping concentration and excitation wavelength. Additionally, the maximum S_a and S_r values of the developed NTE microparticles are 0.017 K^{-1} and 0.32% K^{-1}, respectively, at 363 K, revealing their promising applications in ratiometric thermometers. Our findings provide a facile approach for the future development of highly sensitive optical thermometers.

Conflicts of interest

There are no conflicts to declare.

Acknowledgements

This work was supported by the K. C. Wong Magna Fund in Ningbo University (xkzw 1507), Fundamental Research Funds for the Provincial Universities of Zhejiang (SJLZ2020004) and key research and development plan of Zhejiang Province (2019C04009).

Notes and references

1 H. Suo, X. Zhao, Z. Zhang, Y. Wang, J. Sun, M. Jin and C. Guo, *Laser Photonics Rev.*, 2020, **15**, 2000319.
2 X. Li, C. Yang, Y. Yu, Z. Li, J. Lin, X. Guan, Z. Zheng and D. Chen, *ACS Appl. Mater. Interfaces*, 2020, **12**, 18705–18714.
3 T. P. Swieten, D. Yu, T. Yu, S. J. W. Vonk, M. Suta, Q. Zhang, A. Meijerink and F. T. Rabouw, *Adv. Opt. Mater.*, 2021, **9**, 2001518.
4 Z. Sun, M. Jia, Y. Wei, J. Cheng, T. Sheng and Z. Fu, *Chem. Eng. J.*, 2020, **381**, 122654.
5 K. Maciejewska, A. Bednarkiewicz, A. Meijerink and L. Marciniak, *J. Phys. Chem. C*, 2021, **125**, 2659–2665.
6 J. Zhang and F. Qian, *Dalton Trans.*, 2020, **49**, 10949–10957.
7 M. Runowski, P. Woźny, N. Stopikowska, I. R. Martín, V. Lavín and S. Lis, *ACS Appl. Mater. Interfaces*, 2020, **12**, 43933–43941.
8 L. Luo, W. Ran, P. Du, W. Li and D. Wang, *Adv. Mater. Interfaces*, 2020, **7**, 1902208.
9 F. Huang and D. Chen, *J. Mater. Chem. C*, 2017, **5**, 5176–5182.
10 Z. Zheng, J. Zhang, X. Liu, R. Wei, F. Hu and H. Guo, *Ceram. Int.*, 2020, **46**, 6154–6159.
11 H. Zhang, Y. Liang, H. Yang, S. Liu, H. Li, Y. Gong, Y. Chen and G. Li, *Inorg. Chem.*, 2020, **59**, 14337–14346.
12 J. Xue, H. Mi Noh, B. C. Choi, S. H. Park, J. H. Kim, J. H. Jeong and P. Du, *Chem. Eng. J.*, 2020, **382**, 122861.
13 L. Dong, L. Zhang, Y. Jia, Y. Xu, S. Yin and H. You, *Inorg. Chem.*, 2020, **59**, 15969–15976.
14 C. Wang, Y. Jin, L. Yuan, H. Wu, G. Ju, Z. Li, D. Liu, Y. Lv, L. Chen and Y. Hu, *Chem. Eng. J.*, 2019, **374**, 992–1004.
15 Y. Chen, J. He, X. Zhang, M. Rong, Z. Xia, J. Wang and Z. Liu, *Inorg. Chem.*, 2020, **59**, 1383–1392.
16 L. Li, G. Tian, Y. Deng, Y. Wang, Z. Cao, F. Ling, Y. Li, S. Jiang, G. Xiang and X. Zhou, *Opt. Express*, 2020, **28**, 33747–33756.
17 P. Du, J. Tang, W. Li and L. Luo, *Chem. Eng. J.*, 2021, **406**, 127165.
18 H. Yuan, C. Wang, Q. Gao, X. Ge, H. Sun, S. H. Lapidus, J. Guo, M. Chao, Y. Jia and E. Liang, *Inorg. Chem.*, 2020, **59**, 4090–4095.
19 H. Ishizaki, Y. Sakai, T. Nishikubo, Z. Pan, K. Oka, H. Yamamoto and M. Azuma, *Chem. Mater.*, 2020, **32**, 4832–4837.
20 H. Zou, B. Chen, Y. Hu, Q. Zhang, X. Wang and F. Wang, *J. Phys. Chem. Lett.*, 2020, **11**, 3020–3024.
21 H. Zou, X. Yang, B. Chen, Y. Du, B. Ren, X. Sun, X. Qiao, Q. Zhang and F. Wang, *Angew. Chem., Int. Ed.*, 2019, **58**, 17255–17259.
22 X. Liu, Y. Cheng, E. Liang and M. Chao, *Phys. Chem. Chem. Phys.*, 2014, **16**, 12848–12857.
23 X. Liu, X. Ge, E. Liang and W. Zhang, *Chin. Phys. B*, 2017, **26**, 118101.
24 X. Liu, X. Chen, Y. Yu, W. Xie, Y. Zhao, S. Luo, G. Mei and J. Lin, *Inorg. Chem.*, 2020, **59**, 12348–12361.
25 X. Li, Y. Yu, J. Hong, Z. Feng, X. Guan, D. Chen and Z. Zheng, *J. Lumin.*, 2020, **219**, 116897.
26 C. Wang, P. Du, L. Luo and W. Li, *J. Lumin.*, 2021, **233**, 117896.

27 S. Kaur, A. S. Rao and M. Jayasimhadri, *Mater. Res. Bull.*, 2019, **116**, 79–88.
28 P. Du, Y. Hou, W. Li and L. Luo, *Dalton Trans.*, 2020, **49**, 10224–10231.
29 X. Huang, J. Liang, S. Rtimi, B. Devakumar and Z. Zhang, *Chem. Eng. J.*, 2021, **405**, 126950.
30 D. Huang, Y. Wei, P. Dang, X. Xiao, H. Lian and J. Lin, *J. Am. Ceram. Soc.*, 2020, **103**, 3273–3285.
31 J. Zhao, X. Wang, L. Li and C. Guo, *Ceram. Int.*, 2020, **46**, 5015–5019.
32 X. Tong, J. Han, R. Cai, Y. Xu, P. Wu, H. Zhou and X. Zhang, *Inorg. Chem.*, 2020, **59**, 9838–9846.
33 Z. Ming, J. Zhao, H. C. Swart and Z. Xia, *J. Rare. Earths*, 2020, **38**, 506–513.
34 H. Chen and Y. Wang, *Inorg. Chem.*, 2019, **58**, 7440–7452.
35 M. Inokuti and F. Hirayama, *J. Chem. Phys.*, 1965, **43**, 1978.
36 M. Shang, G. Li, X. Kang, D. Yang, D. Geng and J. Lin, *ACS Appl. Mater. Interfaces*, 2011, **3**, 2738–2746.
37 C. Zhou, Q. Zhang, S. Liu, B. Luo, E. Yi, E. Tian, G. Li, L. Li and G. Wu, *Phys. Chem. Chem. Phys.*, 2017, **19**, 11778–11785.
38 B. A. Marinkovic, M. Ari, R. R. Avillez, F. Rizzo, F. F. Ferreira, K. J. Miller, M. B. Johnson and M. A. White, *Chem. Mater.*, 2009, **21**, 2886–2894.
39 H. Suo, C. Guo, J. Zheng, B. Zhou, C. Ma, X. Zhao, T. Li, P. Guo and E. M. Goldys, *ACS Appl. Mater. Interfaces*, 2016, **8**, 30312–30319.
40 X. Wang, Y. Wang, Y. Bu, X. Yan, J. Wang, P. Cai, T. Vu and H. J. Seo, *Sci. Rep.*, 2017, **7**, 43383.
41 E. Pan, G. Bai, L. Wang, L. Lei, L. Chen and S. Xu, *ACS Appl. Nano Mater.*, 2019, **2**, 7144–7151.
42 X. Wang, Y. Wang, L. Jin, Y. Bu, X. L. Yang and X. Yan, *J. Alloys Compd.*, 2019, **773**, 393–400.
43 Y. Jiang, Y. Tong, S. Chen, W. Zhang, F. Hu, R. Wei and H. Guo, *Chem. Eng. J.*, 2021, **413**, 127470.
44 K. Li, D. Zhu and H. Lian, *J. Alloys Compd.*, 2020, **816**, 1522554.